Fixed-point tensor is a four-point function

Atsushi Ueda[1,*] and Masahito Yamazaki[2,3,4,†]

[1] *Institute for Solid State Physics, University of Tokyo, Kashiwa 277-8581, Japan*
[2] *Kavli IPMU (WPI), UTIAS, The University of Tokyo, Kashiwa, Chiba 277-8583, Japan*
[3] *Center for Data-Driven Discovery, Kavli IPMU (WPI), UTIAS, The University of Tokyo, Kashiwa, Chiba 277-8583, Japan*
[4] *Trans-Scale Quantum Science Institute, The University of Tokyo, Tokyo 113-0033, Japan*

(Dated: December 23, 2024)

Through coarse-graining, tensor network representations of a two-dimensional critical lattice model flow to a universal four-leg tensor, corresponding to a conformal field theory (CFT) fixed-point. We computed explicit elements of the critical fixed-point tensor, which we identify as the CFT four-point function. This allows us to directly extract the operator product expansion coefficients of the CFT from these tensor elements. Combined with the scaling dimensions obtained from the transfer matrix, we determine the complete set of the CFT data from the fixed-point tensor for any critical unitary lattice model.

Introduction.— Renormalization group (RG) [1–3] is one of the most profound concepts in contemporary physics. RG theory has significantly deepened our understanding of the universality of critical phenomena [4, 5]. We now understand that each universality class is described by an RG fixed-point (FP) theory under the RG transformation, which theory can be represented [6, 7] as a conformal field theory (CFT) [8]. Universal behavior, such as critical exponents, can then be elucidated from the CFT data, which include central charges, scaling dimensions, and operator product expansion (OPE) coefficients [9–11]. It is therefore of paramount importance to identify this CFT data for a given ultraviolet (UV) theory (such as a lattice model). [12].

While the analysis of the real-space RG transformation has a long history [13], tensor network renormalization (TNR) [14–20] has recently emerged as a reliable numerical implementation of the real-space RG. The application of TNR has demonstrated that the tensor-network representation of the Boltzmann weights converges to a FP tensor, representing the RG fixed point.

There are several motivations for studying the FP tensors.

First, we expect that the FP tensor encodes the CFT data of the FP theory. Gu and Wen have established a method for calculating the central charge and scaling dimensions for fixed-point tensors, a procedure that has since become standard [21]. It remains an intricate and challenging problem, however, to compute the OPE coefficients of the FP CFT [22–25].

Second, determination of the fixed-point tensor can facilitate concrete realizations of the RG flow. Recently, Kennedy and Rychkov initiated a rigorous study of the RG using tensor networks [26, 27]. Employing simple low-temperature and high-temperature fixed-point tensors, they successfully demonstrated the stability of the corresponding fixed points. Nevertheless, the application of similar arguments to critical fixed points remains unachieved, given that even their tensor network representations are not fully understood.

Third, precise expressions of the fixed-point tensors will serve as a robust benchmark for evaluating the precision of different tensor-network algorithms. A number of algorithms boasting increased accuracy have been developed to determine the FP tensor, but there remain uncertainties in selecting the superior option due to our limited understanding of the exact expression of the fixed-point tensor.

In this Letter, we introduce an exact tensor network representation of critical RG fixed points, thereby solving the problem of numerically determining the full defining data of the FP CFT. We anticipate that our findings will serve as a pivotal contribution in practical computations of the FP theory on the one hand, and towards the rigorous substantiation of RG theory, on the other.

Fixed-point tensor.— To simulate two-dimensional statistical models, we use the tensor network methods, where the local Boltzmann weight is represented as a four-legged tensor $T^{(0)}$. We obtain the transfer matrix in the y-direction if we contract L copies of the four-leg tensors along a circle in the x-direction; we obtain the partition function $Z(L, T^{(0)})$ if we contract $L \times L$ copies along the torus in the x, y-directions. In practical simulations, the exact contraction of two-dimensional tensor networks is notoriously challenging, often proving to be exponentially hard. To address this, we consider a tensor RG map that effectively coarse-grains the local tensors, as illustrated below:

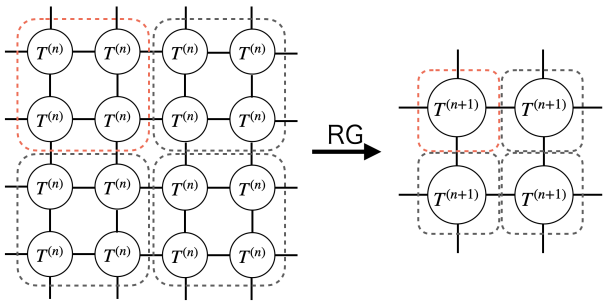

In the initial RG step, we apply the RG map to the original Boltzmann tensor, denoted as $T^{(0)}$, to yield $T^{(1)}$. Subsequently, $T^{(1)}$ is used to generate the next tensor in the sequence. This RG map is designed to ensure that the renormalized tensor remains a close approximation of the original tensor group, while selectively discarding local entanglement. While the specifics of the technical implementation vary depending on the chosen algorithms, it is established that $T^{(n)}$ converges to a universal tensor, T^*, at critical points. This universally convergent tensor, T^*, is referred to as the FP tensor. Its significance lies in its close association with the RG fixed-point, reflecting the underlying principles of scale invariance and universality in the renormalization group theory.

If the original tensor $T^{(0)}$ has D_4 symmetry(reflection and $\pi/2$ rotation), T^* also respects it. This allows the decomposition of the FP tensor into a pair of two identical three-leg tensors S^*:

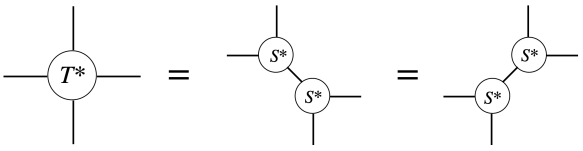

(1)

The FP tensor T^* has gauge degrees of freedom that change the basis of each leg. The insertion of the gauge transformation (unitary operators) does not change the spectral property of the FP tensor. In the following, we fix the gauge so that each index of the FP tensor is labeled by the eigenstates of the Hamiltonian $L_0 + \bar{L}_0$ on a cylinder, where L_n ($\bar{L}_n$) are the standard generators of the left-moving (right-moving) Virasoro algebras. By the state-operator correspondence, we can label these states by a set of operators ϕ_α, among which we will find the identity operator ϕ_1 with the lowest scaling dimension. [28] In tensor-network representations, the projector to this basis can be found by diagonalizing the transfer matrix as follows [21]:

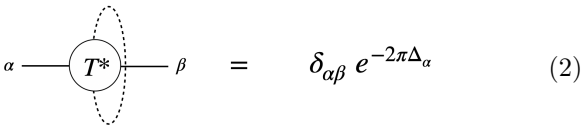

(2)

In the following, we choose the states $\alpha, \beta, \ldots$ to be primary operators.

Main Results.— Let us now state the main results of this paper. First, the three-leg tensor S^* is proportional to the three-point functions of the FP CFT on the complex plane:

$$\frac{S^*_{\alpha\beta\gamma}}{S^*_{111}} = \langle \phi_\alpha(-x_S)\phi_\beta(ix_S)\phi_\gamma(0)\rangle_{\rm pl}. \tag{3}$$

Second, the four-leg FP tensor determines the four-point functions of the FP CFT as

$$\frac{T^*_{\alpha\beta\gamma\delta}}{T^*_{1111}} = \langle \phi_\alpha(-x_T)\phi_\beta(ix_T)\phi_\gamma(x_T)\phi_\delta(-ix_T)\rangle_{\rm pl}. \tag{4}$$

These equalities hold when we choose the values $x_S = e^{\pi/4}$ and $x_T = e^{\pi/2}/2$.

We can now reproduce the *full* defining data for the FP CFT. Recall that we can extract the scaling dimensions Δ_α operators from Eq. (2). The remaining data is the OPE coefficients $C_{\alpha\beta\gamma}$ of the operators ϕ_α, which can be extracted by applying a conformal transformation to Eq. (3):

$$\begin{aligned}\frac{S^*_{\alpha\beta\gamma}}{S^*_{111}} &= \frac{C_{\alpha\beta\gamma}}{x_S^{\Delta_\beta+\Delta_\gamma-\Delta_\alpha} x_S^{\Delta_\gamma+\Delta_\alpha-\Delta_\beta} (\sqrt{2}x_S)^{\Delta_\alpha+\Delta_\beta-\Delta_\gamma}}, \\ &= \frac{2^{\Delta_\gamma} C_{\alpha\beta\gamma}}{(\sqrt{2}x_S)^{\Delta_\alpha+\Delta_\beta+\Delta_\gamma}}. \end{aligned} \tag{5}$$

Equation (1) represents the equivalence of two different decompositions (s- and t-channels) of the four-point function into a pair of three-point functions, i.e. the celebrated crossing relation of the CFT.

To better understand Eqs. (3-4), we apply conformal transformations to the two equations to obtain

$$\frac{S^*_{\alpha\beta\gamma}}{S^*_{111}} = e^{-\frac{\pi}{4}(\Delta_\alpha+\Delta_\beta+\Delta_\gamma)} \langle \phi_\alpha(-1)\phi_\beta(i)\phi_\gamma(0)\rangle_{\rm pl}, \tag{6}$$

$$\frac{T^*_{\alpha\beta\gamma\delta}}{T^*_{1111}} = \left(\frac{e^{\frac{\pi}{2}}}{2}\right)^{-\Delta_{\rm tot}} \langle \phi_\alpha(-1)\phi_\beta(i)\phi_\gamma(1)\phi_\delta(-i)\rangle_{\rm pl}, \tag{7}$$

where $\Delta_{\rm tot} \equiv \Delta_\alpha + \Delta_\beta + \Delta_\gamma + \Delta_\delta$.

Equations (6-7) naturally arise from the following arguments. Once we fix the basis for the FP tensor, each index corresponds to the states of CFT. Thus, the tensor elements of the FP tensor are the coefficients of each basis:

$$T^* = T^*_{\alpha\beta\gamma\delta} |\phi_\alpha\rangle |\phi_\beta\rangle |\phi_\gamma\rangle |\phi_\delta\rangle \tag{8}$$

On the other hand, the FP tensor itself is a lattice representation of the identity operator 1. In Ref. [22, 25, 29], they confirmed that local scale-transformation could be realized using the FP tensors.

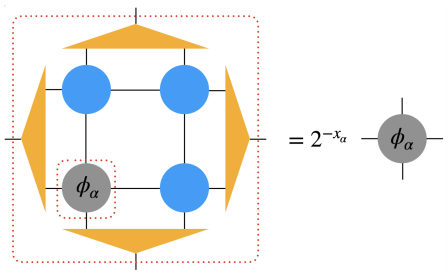

The scale transformation of a four-leg tensor, comprising the FP tensor (colored blue) and isometry (colored orange), results in primary operators emerging as eigenstates. Notably, the scale-invariant FP tensor corresponds to $x_\alpha = 0$. This specific correspondence is significant, equating the FP tensor to the identity operator [30]. This observation leads us to a conceptualization where

the elements of the tensor can be expressed as an overlap between the four-leg identity operator and four one-leg primary operators as $T^*_{\alpha\beta\gamma\delta} = \langle\phi_\alpha\phi_\beta\phi_\gamma\phi_\delta|\phi_1^{4-leg}\rangle$. The same argument can be applied to the three-leg FP tensor S^*. To calculate these values, we employ a technique similar to the one described in the referenced literature, specifically in Ref. [31, 32].

First, utilizing state-operator correspondence, the normalized wave function of the first index of S^*, for instance, is created by inserting ϕ_α in the future infinity of the cylinder as follows:

$$|\phi^1\rangle = \left(\frac{2\pi}{L}\right)^{-\Delta_\alpha} \lim_{z\to\infty} e^{2\pi z\Delta_\alpha/L}\phi_\alpha(\infty)|I^{\rm cyl}\rangle,$$

where $|I^{\rm cyl}\rangle$ represents the ground state corresponding to the identity operator. Subsequently, the FP tensors S^* and T^* can be expressed by the path integral on the manifolds Σ_S and Σ_T, respectively, as illustrated in Fig. 1. Then, the FP-tensor elements are

$$\frac{S^*_{\alpha\beta\gamma}}{S^*_{111}} = \langle\phi_\alpha(\infty)\phi_\beta(i\infty)\phi_\gamma(-(1+i)\infty)\rangle_{\Sigma_S}, \quad (9)$$

$$\frac{T^*_{\alpha\beta\gamma\delta}}{T^*_{1111}} = \langle\phi_\alpha(-\infty)\phi_\beta(i\infty)\phi_\gamma(\infty)\phi_\delta(-i\infty)\rangle_{\Sigma_T}. \quad (10)$$

Σ_S and Σ_T can be mapped the complex plane w by using Mandelstam mapping [33, 34],

$$z_S = \frac{L}{2\pi}[-\ln(w-i) - i\ln(w+1) + (1+i)\ln w], \quad (11)$$

$$z_T = \frac{L}{2\pi}\left[\ln\left(\frac{w+i}{w-i}\right) + i\ln\left(\frac{w-1}{w+1}\right)\right]. \quad (12)$$

Each operator in the z-coordinate transforms accordingly as

$$\frac{S^*_{\alpha\beta\gamma}}{S^*_{111}} = \langle\phi_\alpha(-1)\phi_\beta(i)\phi_\gamma(0)\rangle_{\rm pl} \prod_{n\in(\alpha,\beta,\gamma)} |J_n|^{\Delta_n},$$

$$\frac{T^*_{\alpha\beta\gamma\delta}}{T^*_{1111}} = \langle\phi_\alpha(-1)\phi_\beta(i)\phi_\gamma(1)\phi_\delta(-i)\rangle_{\rm pl} \prod_{n\in(\alpha,\beta,\gamma,\delta)} |J_n|^{\Delta_n},$$

where $|J_n| = |\left(\frac{2\pi}{L}\right)^{-1} \lim_{z\to\zeta\infty} e^{2\pi z\zeta^*/(L|\zeta|)}|w'(z)|$, and $\zeta\infty$ is the coordinate of the index in the original manifold. The resulting $|J_n|$ are $e^{-\pi/4}$ and $2e^{-\pi/2}$, respectively, being consistent with Eqs. (6-7). Detailed calculations are presented in the supplemental material.

Numerical fixed point tensor.— Let us provide numerical confirmations of our main results using Levin's tensor renormalization group (TRG) [14] and Evenbly's TNR [17]. TRG and TNR are numerical techniques that calculate effective $L\times L$ tensor networks. In our study, our interest lies in computing those of large system sizes to obtain a tensor that is as close as possible to the FP tensor. However, performing an exact contraction is exponentially difficult, prompting us to focus on extracting low-lying spectral properties. TRG/TNR seeks to circumvent this issue by employing the principles of the renormalization group theory. Each coarse-graining step entails decompositions and recombinations. Truncation, parameterized by the bond dimension D, is performed to maintain the tractability of numerical computation. However, it is important to note that this scheme is considered *exact* when $D=\infty$, and thus, employing larger D improves the numerical accuracy. Additionally, we impose special D_4 symmetry in TRG. The details can be found in the supplemental material. It is crucial to acknowledge that the TRG method is known to exhibit instabilities, primarily due to its inherent limitations in eliminating certain types of local entanglement. In contrast, TNR, which includes a local entanglement filtering process, typically demonstrates superior performance in extracting infra-red information. This enhanced capability of TNR is attributed to its more effective handling of local entanglement, making it a more robust approach for studying systems at criticality.

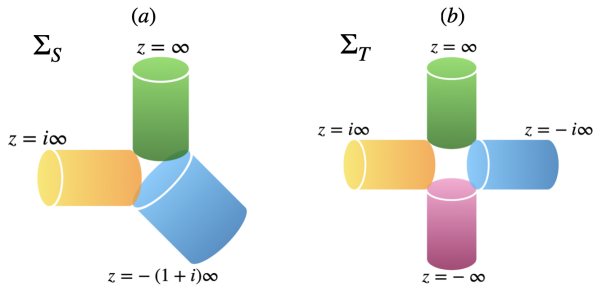

FIG. 1. The path-integral representation of the tensor elements (*a*) $S^*_{\alpha\beta\gamma}$ and (*b*) $T^*_{\alpha\beta\gamma\delta}$. The fixed-point tensor lives at the center of cylinders, and surrounding cylinders are bra vectors of primary fields. Since the FP tensor corresponds to the identity operator, "insertion of no operator" is illustrated as empty space. This identity operator at the origin in z coordinate will be mapped to the infinity in w.

Tests on critical lattice models.—Let us first test the value $x_S = e^{\pi/4}$ in Eq. (6), by computing x_S from the critical Ising and 3-state Potts models. Given Eq. (6), we can numerically compute the OPE coefficients $C_{\alpha\beta\gamma}$ from Eq. (5). We define $x_S(L)$ by solving Eq. (5) to be

$$x_S(L) \equiv \frac{1}{\sqrt{2}}\left(\frac{2^{\Delta_\gamma}C_{\alpha\beta\gamma}}{S_{\alpha\beta\gamma}(L)}\right)^{1/(\Delta_\alpha+\Delta_\beta+\Delta_\gamma)}. \quad (13)$$

Each model has a primary operator ϵ, called the energy and the thermal operator, respectively. Since $C_{\epsilon\epsilon 1} = 1$, $x_S(L)$ can be computed from the finite-size three-leg tensor $S_{\epsilon\epsilon 1}(L)$.

Figure 2 shows the value of $x_S(L)$ obtained from TRG and TNR at the bond dimension $D=96$ and $D=40$, respectively. The numerically derived $x_S(L)$'s for both models converge to the theoretical value of $e^{\pi/4}$. The noticeable increase in amplitude for the 3-state Potts model

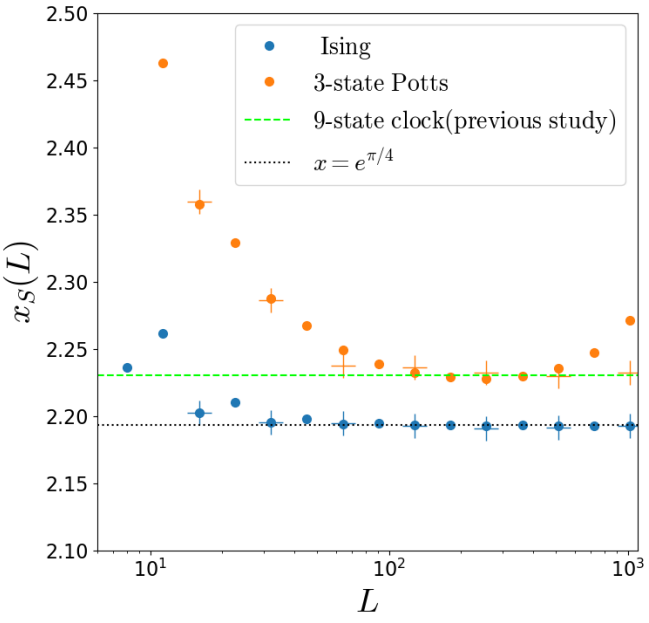

FIG. 2. Estimation of $x_S(L)$ from Levin-TRG($D = 96$) and Evenbly-TNR($D = 40$). The values of $x(L)$ from the Ising and 3-state Potts model converge to the theoretical value $x_S = e^{\pi/4}$ denoted by a black dotted line. We plot $x_S = 2.23035$ obtained from Loop-TNR [17] on the critical 9-state clock model [23] with a lime dashed line. The 3-state Potts model exhibits a deviation for $L > 100$ because simulating systems with higher central charges involves larger numerical errors.

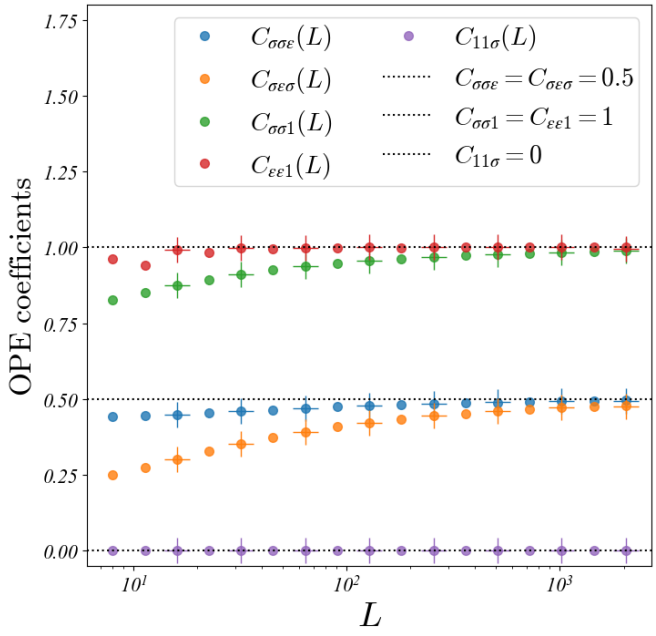

FIG. 3. The OPE coefficients of the critical Ising model evaluated by setting $x_S = e^{\pi/4}$. The black dotted lines denote the theoretical values 0, 0.5, and 1. The data points, denoted by filled circles "∘" and crosses "+," are obtained from Levin-TRG($D = 96$) and Evenbly-TNR($D = 40$), respectively.

by TRG at $L > 10^2$ is attributed to the effect of the finite bond dimension and the remaining local entanglement. It is worth noting that our value for x_S deviates slightly from the value $x_S = 2.23035$ [35] from a previous study on the 9-state clock model [23]. We speculate that this minor deviation is due to the finite bond-dimension effect because higher central charges lead to more pronounced numerical errors [24]. For the system size $L = 2048$ and bond dimension $D = 96$, we ascertain $x_S = 2.193257$ for the Ising model, a value remarkably close to $e^{\pi/4} = 2.193280$. Once we are certain of the value $x_S = e^{\pi/4}$, we can verify Eq. (6) for all the OPE coefficients, which are computed from the three-leg tensor S as

$$C_{\alpha\beta\gamma}(L) = (\sqrt{2}\, e^{\pi/4})^{\Delta_\alpha+\Delta_\beta+\Delta_\gamma} 2^{-\Delta_\gamma} S_{\alpha\beta\gamma}(L). \quad (14)$$

The results for the critical Ising model are exhibited in Fig. 3. The obtained OPE coefficients are consistent with our theory with the finite-size effects of expected scaling. The finite-size effect originates from the twist operator at the branch points [31, 32], whose scaling is universal. The detailed analysis is discussed in the supplemental material. The same plot for the critical three-state Potts model is shown in the supplemental material. While it has less accuracy due to the stronger finite bond dimension effect for higher central charges, the result is still consistent with the expected OPE coefficients.

We next computed four-point tensors $T_{\alpha\beta\gamma\delta}$ and compared with the theoretical values from Eq. (7), where the explicit forms of the four-point functions of the critical Ising model are listed in the supplemental material. The result is consistent up to two digits for most tensor elements, as shown in Table I. The exceptions are $T_{\sigma\sigma\sigma\sigma}$ and $T_{\sigma\sigma 11}$, whose numerical values deviate approximately 5% from the theoretical values. As for $T_{\sigma\sigma\epsilon 1}$, the deviation is almost 24% [36]. This discrepancy, however, can be attributed to finite-size effects and becomes negligible for infinite system sizes. To illustrate this, we define the finite-size deviation as (do not confuse with temperature)

$$\delta T_{\alpha\beta\gamma\delta} \equiv T^*_{\alpha\beta\gamma\delta} - T_{\alpha\beta\gamma\delta}(L).$$

Figure 4 presents the values of $\delta T_{\sigma\sigma\sigma\sigma}(L)$, $\delta T_{\sigma\sigma\epsilon 1}(L)$, and $\delta T_{\sigma\sigma 11}(L)$ obtained from TRG calculations. A clear power-law decay with respect to the system size is observed, supporting the claim that the large deviations for those elements are finite-size effects. However, it is worth mentioning that the exponent closely approximates $\sim L^{-1/3}$, hinting at the existence of an underlying theory that might account for this.

Acknowledgement— We would like to thank Jacob Bridgeman, Clement Delcamp, Jutho Haegeman, Rui-Zhen Huang, Kansei Inamura, Andreas Läuchli, Laurens Lootens, Masaki Oshikawa, Slava Rychkov, Luca Tagliacozzo, Frank Verstraete and Yunqin Zheng for helpful

TABLE I. The comparison of the numerically-obtained fixed-point tensor $T_{\alpha\beta\gamma\delta}$ at $L = 2048$ and the exact four-point function $\langle\phi_\alpha(-x_T)\phi_\beta(ix_T)\phi_\gamma(x_T)\phi_\delta(-ix_T)\rangle_{\rm pl}$ of the Ising model with $x_T = e^{\pi/2}/2$.

	$T_{\alpha\beta\gamma\delta}$ $(L = 2048)$	$\langle\phi_\alpha\phi_\beta\phi_\gamma\phi_\delta\rangle$
1111	1	1
$\sigma\sigma\sigma\sigma$	0.610	0.645
$\sigma\sigma\epsilon\epsilon$	0.0714	0.0716
$\sigma\epsilon\sigma\epsilon$	0.000	0
$\epsilon\epsilon\epsilon\epsilon$	0.0168	0.0168
$\sigma\sigma\epsilon 1$	0.0618	0.0765
$\sigma\epsilon\sigma 1$	0.133	0.140
$\sigma\sigma\sigma 1$	0.000	0
$\epsilon\epsilon\epsilon 1$	0.001	0
$\sigma\sigma 11$	0.708	0.736
$\sigma 1\sigma 1$	0.639	0.675
$\epsilon\epsilon 11$	0.0863	0.0864
$\epsilon 1\epsilon 1$	0.0439	0.0432
$\epsilon\sigma 11$	0.000	0

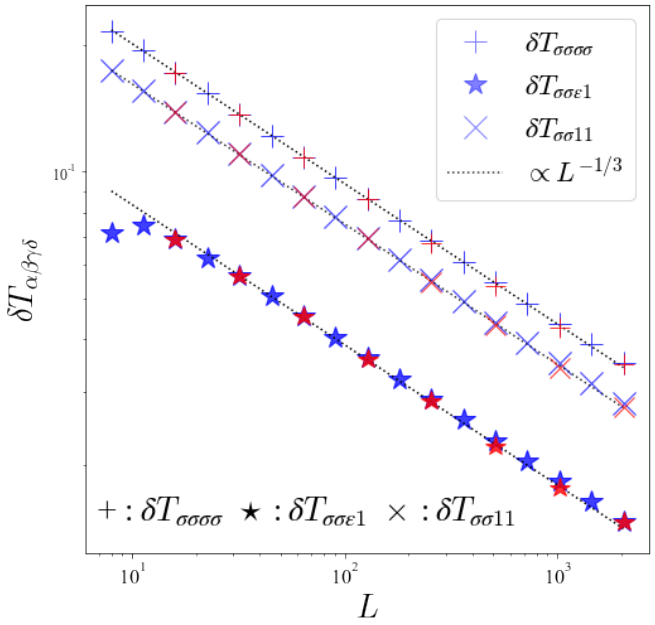

FIG. 4. The finite-size effect of the fixed point tensor $\delta T_{\alpha\beta\gamma\delta} \equiv \langle\phi_\alpha\phi_j\beta\phi_\gamma\phi_\delta\rangle - T_{\alpha\beta\gamma\delta}(L)$ from Levin-TRG($D = 96$, red) and Evenbly-TNR($D = 40$, blue). We plot $\delta T_{\alpha\beta\gamma\delta}$ of $\sigma\sigma\sigma\sigma$("+"), $\sigma\sigma\epsilon 1$("⋆"), and $\sigma\sigma 11$("×") with different colors depending on the algorithm. The difference converges to zero for $L \to \infty$ with the power-law $\sim L^{-1/3}$.

discussions. A. U. is supported by the MERIT-WINGS Program at the University of Tokyo, the JSPS fellowship (DC1). He was supported in part by MEXT/JSPS KAKENHI Grants No. JP21J2052. M. Y. was supported in part by the JSPS Grant-in-Aid for Scientific Research (19H00689, 19K03820, 20H05860, 23H01168), and by JST, Japan (PRESTO Grant No. JPMJPR225A, Moonshot R&D Grant No. JPMJMS2061). *Source Availability.*– Our numerical data and analysis codes for the Ising fixed-point are publicly available at `https://github.com/dartsushi/TRG_D4_symmetry`.

* aueda@issp.u-tokyo.ac.jp
† masahito.yamazaki@ipmu.jp

[1] E. Stuckelberg and A. Petermann, Helv. Phys. Acta **24**, 317 (1951); **26**, 499 (1953).
[2] M. Gell-Mann and F. E. Low, Phys. Rev. **95**, 1300 (1954).
[3] N. Bogolubov and D. Shirkov, Dokl. Acad. Nauk SSSR **103**, 203 (1955); **105**, 685 (1955).
[4] K. G. Wilson and J. B. Kogut, Phys. Rept. **12**, 75 (1974).
[5] L. P. Kadanoff, Rev. Mod. Phys. **49**, 267 (1977).
[6] J. Polchinski, Nucl. Phys. B **303**, 226 (1988).
[7] M. A. Luty, J. Polchinski, and R. Rattazzi, Journal of High Energy Physics **2013**, 10.1007/jhep01(2013)152 (2013).
[8] A. A. Belavin, A. M. Polyakov, and A. B. Zamolodchikov, Nucl. Phys. B **241**, 333 (1984).
[9] J. Cardy, *Scaling and renormalization in statistical physics*, Vol. 5 (Cambridge university press, 1996).
[10] P. Di Francesco, P. Mathieu, and D. Senechal, *Conformal Field Theory*, Graduate Texts in Contemporary Physics (Springer-Verlag, New York, 1997).
[11] J. Zinn-Justin, *Quantum field theory and critical phenomena*, Vol. 171 (Oxford university press, 2021).
[12] The conformal bootstrap [37–40] is a notable technique that has successfully computed the CFT data for e.g. the three-dimensional Ising model to a high precision [41]. Despite its successes, the main focus of the conformal bootstrap is to constrain the possible parameter spaces of CFTs, and it is often not sufficient if one wishes to calculate the CFT data for a specific lattice model. In this sense, our results complement the bootstrap program.
[13] L. P. Kadanoff, Physics Physique Fizika **2**, 263 (1966).
[14] M. Levin and C. P. Nave, Phys. Rev. Lett. **99**, 120601 (2007).
[15] G. Evenbly and G. Vidal, Phys. Rev. Lett. **115**, 180405 (2015).
[16] G. Evenbly, Phys. Rev. B **95**, 045117 (2017).
[17] S. Yang, Z.-C. Gu, and X.-G. Wen, Phys. Rev. Lett. **118**, 110504 (2017).
[18] M. Bal, M. Mariën, J. Haegeman, and F. Verstraete, Phys. Rev. Lett. **118**, 250602 (2017).
[19] M. Hauru, C. Delcamp, and S. Mizera, Phys. Rev. B **97**, 045111 (2018).
[20] K. Homma and N. Kawashima, Nuclear norm regularized loop optimization for tensor network (2023), arXiv:2306.17479 [cond-mat.stat-mech].
[21] Z.-C. Gu and X.-G. Wen, Phys. Rev. B **80**, 155131 (2009).
[22] G. Evenbly and G. Vidal, Phys. Rev. Lett. **116**, 040401 (2016).
[23] G. Li, K. H. Pai, and Z.-C. Gu, Phys. Rev. Res. **4**, 023159 (2022).
[24] A. Ueda and M. Oshikawa, Phys. Rev. B **108**, 024413 (2023).
[25] W. Guo and T.-C. Wei, Tensor network methods for extracting cft data from fixed-point tensors and defect coarse graining (2023), arXiv:2305.09899 [cond-mat.stat-

mech].
[26] T. Kennedy and S. Rychkov, Journal of Statistical Physics **187**, 10.1007/s10955-022-02924-4 (2022).
[27] T. Kennedy and S. Rychkov, Tensor renormalization group at low temperatures: Discontinuity fixed point (2023), arXiv:2210.06669 [math-ph].
[28] Note that the label α refers to both the primaries and the descendants of the Virasoro algebra.
[29] X. Lyu, R. G. Xu, and N. Kawashima, Phys. Rev. Res. **3**, 023048 (2021).
[30] Unitary CFTs have ground states corresponding to the identity operator.
[31] Y. Liu, Y. Zou, and S. Ryu, Phys. Rev. B **107**, 155124 (2023).
[32] Y. Zou and G. Vidal, Phys. Rev. B **105**, 125125 (2022).
[33] S. Mandelstam, Nucl. Phys. B **64**, 205 (1973).
[34] Y. Baba, N. Ishibashi, and K. Murakami, Journal of High Energy Physics **2009**, 010–010 (2009).
[35] Their paper showed that the three-leg FP tensor $S*$ had the same structure as a three-point function by numerical experiments. In this process, they treat x_S as a fitting parameter to reproduce known OPE coefficients. Our results show that they are indeed three-point functions and x_S is a universal number and not a fitting parameter.
[36] The TNR scheme has a similar performance at the same length-scale as seen in Fig. 4.
[37] S. Ferrara, A. F. Grillo, and R. Gatto, Annals Phys. **76**, 161 (1973).
[38] A. M. Polyakov, Zh. Eksp. Teor. Fiz. **66**, 23 (1974).
[39] R. Rattazzi, V. S. Rychkov, E. Tonni, and A. Vichi, Journal of High Energy Physics **2008**, 031–031 (2008).
[40] D. Poland, S. Rychkov, and A. Vichi, Rev. Mod. Phys. **91**, 015002 (2019).
[41] S. El-Showk, M. F. Paulos, D. Poland, S. Rychkov, D. Simmons-Duffin, and A. Vichi, Phys. Rev. D **86**, 025022 (2012), arXiv:1203.6064 [hep-th].

Supplemental material

Atsushi Ueda and Masahito Yamazaki
(Dated: December 23, 2024)

We provide detailed calculations and algorithms of the conformal mappings and TRG, respectively, in the main text. In addition, we discuss the universal finite-size correction of the tensor elements.

A. Conformal mapping of S

The three-leg tensor $S^*_{\alpha\beta\gamma}$ represents the three-sided thermofield double state [1] corresponding to the geometry in Fig. 1(a) in the main text. This manifold Σ_S is mapped to the plane by a conformal mapping

$$z = \frac{L}{2\pi}[-\ln(w-i) - i\ln(w+1) + (1+i)\ln w], \tag{1}$$

which maps the three points in Σ_S, $(z_1, z_2, z_3) = (\infty, i\infty, -(1+i)\infty)$, to $(w_1, w_2, w_3) = (i, -1, 0)$. Then, the tensor element is

$$\frac{S^*_{\alpha\beta\gamma}}{S^*_{111}} = |J_1|^{\Delta_\alpha}|J_2|^{\Delta_\beta}|J_3|^{\Delta_\gamma}\langle\phi_\alpha(-1)\phi_\beta(i)\phi_\gamma(0)\rangle_{\rm pl}, \tag{2}$$

where J_i is the Jacobian of the conformal mapping (1). The initial states are

$$\begin{aligned}
|\phi^1\rangle &= \left(\frac{2\pi}{L}\right)^{-\Delta_\alpha} \lim_{z\to\infty} e^{2\pi z\Delta_\alpha/L}\phi_\alpha(z)|I^{\rm cyl}\rangle,\\
|\phi^2\rangle &= \left(\frac{2\pi}{L}\right)^{-\Delta_\beta} \lim_{z\to i\infty} e^{-i2\pi z\Delta_\beta/L}\phi_\beta(z)|I^{\rm cyl}\rangle,\\
|\phi^3\rangle &= \left(\frac{\sqrt{2}\pi}{L}\right)^{-\Delta_\gamma}\\
&\quad \lim_{z\to(-i-1)\infty} e^{\frac{(i-1)}{\sqrt{2}}\frac{2\pi}{\sqrt{2}L}z\Delta_\gamma}\phi_\gamma(z)|I^{\rm cyl}\rangle.
\end{aligned} \tag{3}$$

The Jacobian can be computed as

$$\begin{aligned}
|J_1| &= \left|\left(\frac{2\pi}{L}\right)^{-1} \lim_{z\to\infty} e^{2\pi z/L}w'(z)\right|\\
&= \left|\left(\frac{2\pi}{L}\right)^{-1} \lim_{w\to i} e^{2\pi z/L}\left(\frac{dz}{dw}\right)^{-1}\right|.
\end{aligned} \tag{4}$$

Using Eq. (10) in the main text, the first and second term is

$$e^{2\pi z/L} = \exp[\ln\frac{w}{w-i} + i\ln\frac{w}{w+1}], \tag{5}$$

$$\frac{dz}{dw} = \frac{L}{2\pi}\left[-\frac{1}{w-i} - \frac{i}{w+1} + \frac{(1+i)}{w}\right]. \tag{6}$$

Substituting these into Eq. (4),

$$\begin{aligned}
|J_1| &= \left|\lim_{w\to i}\frac{w}{w-i}\exp\left[i\ln\frac{w}{w+1}\right]\left(\left[-\frac{1}{w-i} - \frac{i}{w+1} + \frac{(1+i)}{w}\right]\right)^{-1}\right|\\
&= \left|\exp\left(i\ln\frac{i}{1+i}\right)\right|\\
&= e^{-\pi/4}.
\end{aligned} \tag{7}$$

In the same way, we can show $|J_2| = |J_3| = e^{-\pi/4}$. Thus, the 3-leg tensor is

$$S^*_{\alpha\beta\gamma} = e^{-\frac{\pi}{4}(\Delta_\alpha+\Delta_\beta+\Delta_\gamma)}\langle\phi_\alpha(-1)\phi_\beta(i)\phi_\gamma(0)\rangle_{\rm pl}. \tag{8}$$

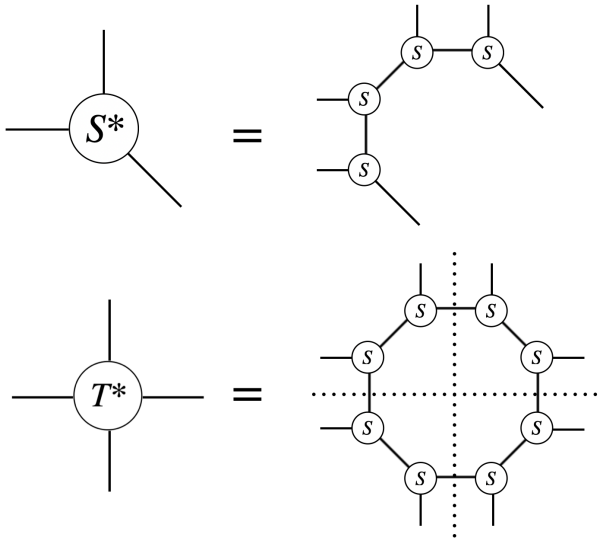

FIG. 1: The contraction of the fixed-point tensors. We obtain S from TRG and combine together to make S^* and T^*. In this way, T^* respects reflection symmetry along the dotted lines in addition to C_4 rotation symmetry.

B. Conformal mapping of T

The conformal mapping from the four-sided thermofield double state is

$$\begin{aligned} z &= \frac{L}{2\pi}[-\ln(w-i)+\log(w+i)-i\ln(w+1)+i\ln(w-1)] \\ &= \frac{L}{2\pi}\left[\ln\left(\frac{w+i}{w-i}\right)+i\ln\left(\frac{w-1}{w+1}\right)\right]. \end{aligned} \tag{9}$$

To compute the Jacobian, we compute

$$e^{2\pi z/L} = \exp\left[\ln\frac{w+i}{w-i}+i\ln\frac{w-1}{w+1}\right], \tag{10}$$

$$\frac{dz}{dw} = \frac{L}{2\pi}\left[-\frac{1}{w-i}+\frac{1}{w+i}-\frac{i}{w+1}+\frac{i}{w-1}\right]. \tag{11}$$

The Jacobian is then computed similarly as before:

$$\begin{aligned} |J_1|^{-1} &= \lim_{w\to i}\left|e^{-2\pi z/L}\left[-\frac{1}{w-i}+\frac{1}{w+i}-\frac{i}{w+1}+\frac{i}{w-1}\right]\right| \\ &= \frac{e^{\pi/2}}{2}. \end{aligned} \tag{12}$$

The four-point function thus transforms as

$$\begin{aligned} \frac{T^*_{\alpha\beta\gamma\delta}}{T^*_{1111}} &= |J_1|^{\Delta_\alpha}|J_2|^{\Delta_\beta}|J_3|^{\Delta_\gamma}|J_4|^{\Delta_\delta}\langle\phi_\alpha(-1)\phi_\beta(i)\phi_\gamma(1)\phi_\delta(-i)\rangle_{\rm pl}, \\ &= \left(\frac{e^{\frac{\pi}{2}}}{2}\right)^{-\Delta_{\rm tot}}\langle\phi_\alpha(-1)\phi_\beta(i)\phi_\gamma(1)\phi_\delta(-i)\rangle_{\rm pl}. \end{aligned} \tag{13}$$

C. D_4-symmetric TRG

We use the TRG scheme which aligns closely with the original paper's methodology [2]. In principle, singular-value decomposition (SVD) of the four-leg tensor should yield two identical symmetric tensors, given the D_4 symmetry of

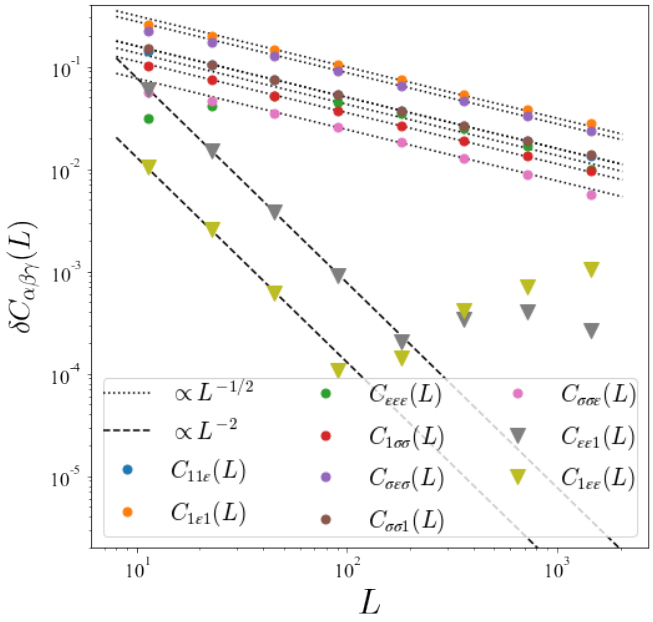

FIG. 2: The finite-size corrections $\delta C_{\alpha\beta\gamma}(L)$ obtained from the numerical simulation of the critical Ising model. The numerical results for higher energy levels $\delta C_{\epsilon\epsilon 1}(L)$ and $\delta C_{1\epsilon\epsilon}(L)$ suffer from finite-D effects for $L > 100$. The scalings of the finite-size corrections are nevertheless universal, which is consistent with Table III in Ref. [3]

the original tensor. However, numerical errors sometimes make these two tensors non-identical. To mitigate this, we consistently select one of the three-leg tensors and supplement the other with its reflection. By adopting this approach, the fixed-point tensors, depicted in Fig. 1, maintain the D_4 symmetry at every RG step by construction.

D. Four-point function of the critical Ising model

Here, we list the four-point function of the Ising model. Given the four coordinates z_i and its cross-ratio $x \equiv (z_{12}z_{34})/(z_{13}z_{24})$, the four-point functions of the Ising CFT are

$$\langle \epsilon^4 \rangle = \left| \left[\prod_{1\le i<j\le 4} z_{ij}^{-\frac{1}{3}} \right] \frac{1-x+x^2}{x^{\frac{2}{3}}(1-x)^{\frac{2}{3}}} \right|^2,$$

$$\langle \sigma^2\epsilon^2 \rangle = \left| \left[z_{12}^{\frac{1}{4}} z_{34}^{-\frac{5}{8}} (z_{13}z_{24}z_{14}z_{23})^{-\frac{3}{16}} \right] \frac{1-\frac{x}{2}}{x^{\frac{3}{8}}(1-x)^{\frac{5}{16}}} \right|^2,$$

$$\langle \sigma^4 \rangle = |z_{13}z_{24}|^{-1/4} \frac{|1+\sqrt{1-x}|+|1-\sqrt{1-x}|}{2|x|^{\frac{1}{4}}|1-x|^{\frac{1}{4}}}.$$

The functions above are used to evaluate the analytic FP tensor elements in the main text.

E. Universal finite-size corrections

Here, we discuss the finite-size corrections to Eq. (13) in the main text. The finite-size corrections of the OPE coefficients are defined as

$$\delta C_{\alpha\beta\gamma}(L) = |C_{\alpha\beta\gamma} - C_{\alpha\beta\gamma}(L)|, \tag{14}$$

where $C_{\alpha\beta\gamma}(L)$ is defined in Eq. (13) in the main text. We found that $\delta C_{\alpha\beta\gamma}(L)$ exhibits a universal power-law decay as

$$\delta C_{\alpha\beta\gamma}(L) \sim L^{-p_{\alpha\beta\gamma}}. \tag{15}$$

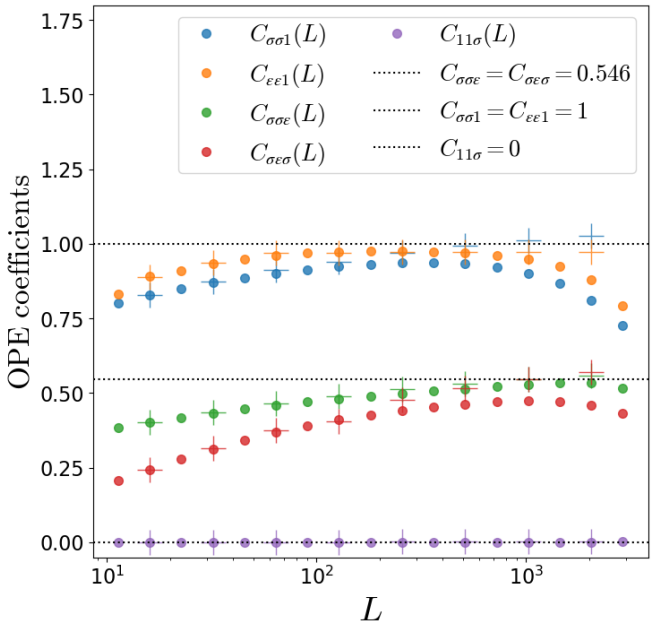

FIG. 3: The OPE coefficients of the critical three-state Potts model evaluated by setting $x_S = e^{\pi/4}$. The black dotted lines denote the theoretical values 0, 0.546, and 1 [4]. The data points, denoted by filled circles "∘" and crosses "+," are obtained from Levin-TRG($D = 88$) and Evenbly-TNR($D = 40$), respectively.

Our numerical results suggest $p_{\alpha\beta\gamma} = 1/2$ for $(\alpha, \beta, \gamma) = (1, 1, \epsilon)$, $(1, \epsilon, 1)$, $(\epsilon, \epsilon, \epsilon)$, $(1, \sigma, \sigma)$, $(\sigma, \epsilon, \sigma)$, $(\sigma, \sigma, 1)$, and $(\sigma, \sigma, \epsilon)$, and $p_{\alpha\beta\gamma} = 2$ for $(\alpha, \beta, \gamma) = (\epsilon, \epsilon, 1)$ and $(1, \epsilon, \epsilon)$ as shown in Fig. 2. Similar universal scalings were discussed in Ref. [3], where they considered the overlap of critical wavefunctions $A_{\alpha\beta\gamma} = \langle \phi^{3*}_{\gamma} | \phi^1_\alpha \phi^2_\beta \rangle$. The three wavefunctions are defined on a ring with a circumference of L_1, L_2, and $L_3 = L_1 + L_2$, respectively, and the lower indices are the label of the corresponding primary states. Ref. [3] found the overlap of wavefunctions to be

$$\frac{A_{\alpha\beta\gamma}}{A_{111}} \sim \left[\left(\frac{L_3}{L_1}\right)^{\frac{L_1}{L_3}} \left(\frac{L_3}{L_2}\right)^{\frac{L_2}{L_3}} \right]^{-\frac{L_3}{L_1}\Delta_\alpha - \frac{L_3}{L_2}\Delta_\beta + \Delta_\gamma} C_{\alpha\beta\gamma} \quad + \quad \tilde{A}^{(p)}_{\alpha\beta\gamma} L_3^{-p_{\alpha\beta\gamma}}, \tag{16}$$

where $p_{\alpha\beta\gamma}$ is the leading finite-size correction and $\tilde{A}^{(p)}_{\alpha\beta\gamma}$ is a prefactor that is independent of L_3.

Our scaling exponents $p_{\alpha\beta\gamma}$ in Eq. (15) coincide with those from the previous work in Eq. (16) for all fusion channels (see Table III of Ref. [3]). This universal scaling can be explained by considering rings 1 and 2 as an orbifold theory. The scaling $p_{\alpha\beta\gamma} = 1/2$ is then attributed to the difference in the scaling dimensions of the orbifold theory, which is $\Delta_\epsilon/2 = 1/2$. (See Ref. [3] for details.) Similarly, we conjecture that the universal scaling for $\delta T_{\alpha\beta\gamma\delta} \sim L^{-1/3}$ can be understood by considering the three of four legs to be an orbifold theory.

I. THE THREE-STATE POTTS MODEL

Here, we present the OPE coefficients obtained from numerical simulations of the classical critical three-state Potts model. The low-lying primary states of this model are the identity operator "1", the two spin operators "σ," and the thermal operator "ϵ," whose scaling dimensions are 0, 2/15, and 4/5. The non-trivial coefficients is $C_{\sigma\sigma\epsilon} = 0.546$ [4]. Figure. 3 exhibits the numerical results from Levin-TRG and Evenbly-TNR as the Ising model in the main text. TRG/TNR schemes, generally speaking, have finite-D effects for larger system sizes, and this effect is larger in higher central charges. Since the central charge $c = 0.8$ of the three-state Potts model is larger than $c = 0.5$ of the Ising model, these numerical errors manifest in the data plots. In particular, the TRG data is unstable due to CDL tensors and quickly diverts from the theoretical values. However, Evenbly-TNR's results still converge to the correct values.

[1] Y. Zou and G. Vidal, Phys. Rev. B **105**, 125125 (2022).
[2] M. Levin and C. P. Nave, Phys. Rev. Lett. **99**, 120601 (2007).
[3] Y. Liu, Y. Zou, and S. Ryu, Phys. Rev. B **107**, 155124 (2023).
[4] J. McCabe and T. Wydro, "Critical correlation functions of the 2-dimensional, 3-state potts model," (1995), arXiv:cond-mat/9507033 [cond-mat] .